7 Summary of the Electronic Spectroscopy of the Au-RG complexes

7.1 Introduction

To complement work on the Au-Ne (Chapter 6), Au-Ar (Chapter 3), Au-Kr (Chapter 4), and Au-Xe (Chapter 5) complexes, additional calculations on Au-He and Au-Rn are introduced allowing trends down the RG series to be discussed. After this discussion, the reader is brought up to date with recent developments in this area of study. A brief description of work from velocity map imaging studies is given, in which the mechanism of predissociation from the $\Xi_{1/2}$ state of Au-Xe is identified along with the directly measured values of D_0'' for the Au-Ar, Au-Kr and Au-Xe complexes. Recent calculations for the Ag-RG and Cu-RG complexes are presented. These results in addition to those obtained for the Au-RG complexes allow trends for the CM-RG species to be commented on. The Chapter ends with concluding remarks for the spectroscopy of the Au-RG complexes and the CM-RG series as a whole.

7.2 Trends down Au-RG series

7.2.1 The $X^2\Sigma^+$ state

To enable comparison of the trends down the whole RG series potential energy curves for the $X^2\Sigma^+$ state of Au-He and Au-Rn were calculated pointwise at the RCCSD(T) level using MOLPRO,[1] it should

be noted that these were performed by other members of the research group. For He, the *d*-awCVXZ (X = Q, 5) basis sets were employed in Au-He. For Au and Rn the relativistic effective core potentials, ECP60MDF[2] were used, to which the aug-cc-pVXZ-PP[3] valence basis set with a further set of primitive diffuse functions of each orbital angular momentum were added. For Au-He all the non-ECP electrons were included in the correlation treatment, while to Au-Rn only the valence electrons were correlated. Each point was corrected for basis set superposition error using the full counterpoise correction,[4] and then extrapolated to the basis limit using the two point extrapolation procedure of Helgaker and co-workers.[5,6] The potential energy curves were used as input for the LEVEL program[7] as described for Au-Ar in Chapter 3. The ^{197}Au, ^{222}Rn and ^{4}He isotopes were used for all calculations. The results of these analyses, along with a summary of the corresponding results from Chapters 3-6 are shown in Table 7.1. It should be noted that in the cases of Au–Ar, Au–Kr and Au–Xe the effect of core-valence correlation which was discussed in the relevant Chapters, is not included here. Since the ground state is considerably lower in energy than the other states, it is not expected that any significant mixing with other states will occur under the influence of spin-orbit coupling, and hence the calculations on the $X^2\Sigma^+$ state should be directly comparable to experiment.

From Table 7.1 it can be seen that, unsurprisingly, the calculated D_e values for the $X^2\Sigma^+$ state of the Au–RG complexes increase as the RG atom becomes heavier, and therefore more polarizable, which is the case for essentially all M–RG and M^+–RG ground-state complexes

studied previously.[8,9] However, even though the van der Waals radii of RG atoms increase steadily and substantially from He to Rn, the R_e values for the Au–RG complexes actually decrease in a regular fashion from He to Rn.

Table 7.1. Calculated spectroscopic constants, and 0-1 and 1-2 vibrational intervals for the $X^2\Sigma^+$ of Au-RG at the RCCSD(T) level of theory.

Basis Set	R_e/ Å	D_e/ cm^{-1}	D_0/ cm^{-1}	0-1 / cm^{-1}	1-2/ cm^{-1}	B_0/ cm^{-1}
			^{197}Au–^{4}He			
d-aVQZ	4.11	14.6	5.7	5.7	---[a]	0.2032
d-aV5Z	4.10	14.9	5.9	5.9	---[a]	0.2052
d-aV∞Z	4.08	15.3	6.1	6.1	---[a]	0.2073
			^{197}Au–^{20}Ne			
d-aV∞Z	3.83	47.2	38.0	15.1	11.0	0.06029
			^{197}Au–^{40}Ar			
d-aV∞Z	3.73	176.5	163.9	23.9	21.9	0.03577
			^{197}Au–^{84}Kr			
d-aV∞Z	3.64	284.8	273.0	22.8	21.8	0.02137
			^{197}Au–^{132}Xe			
d-aV∞Z	3.42	515.5	503.1	24.2	23.7	0.01811
			^{197}Au–^{222}Rn			
d-aVQZ	3.30	704.2	690.0	27.8	27.1	0.00147
d-aV5Z	3.26	758.6	743.4	29.7	28.9	0.00151
d-aV∞Z	3.22	820.3	804.1	31.8	31.0	0.00155

[a] Au–He is only calculated to have two bound levels at the following wavenumbers relative to the asymptote : aCVQZ : -5.7, -0.015 cm^{-1}; aCV5Z : -5.9, -0.022 cm^{-1}; aCV∞Z : -6.1, -0.031 cm^{-1}

This unexpected trend in which R_e decreases as the mass, and hence the size of RG increases, has been observed previously for lighter RG atoms in other M–RG and M$^+$–RG complexes with a single, polarizable *s* electron on M: Na–RG (RG = Ne,[10] Ar[11] and Kr[12]); Group 2 M$^+$–RG ions (Rg = He, Ne and Ar)[8,13]; and Group 12 M$^+$–RG ions (RG = He, Ne and Ar)[14,15]. In some cases, this has been attributed to distortion of the *s*-electron cloud on approach of the RG atom in such a way as to reduce repulsion and thus enhance attraction as R_e decreases and the

RG polarizability increases (see references 8 and 13), but the steady decrease in R_e in the Au–RG cases from He all the way to Rn is quite remarkable. Similar R_e decreases from He to Rn have been very recently observed[9] in *ab initio* calculations of the analogous ground states of Ag–RG and Cu–RG. A further discussion of this trend in R_e for the CM-RG species is given in section 7.4.

Very recently, Cargnoni *et al.*[16] reported a series of calculations on the ground state of the CM-He complexes, using open-shell CCSD(T) and CCSDT calculations, employing large basis sets. Their best values for Au-He are R_e = 4.09 Å and D_e = 15.3 cm^{-1}, both of which are in excellent agreement with the present RCCSD(T)/daV∞Z values (see Table 7.1) adding confidence to the derived parameters; this suggests that the results for the heavier species will also be reliable. Ideally the binding energy of the Au-He complex would be determined experimentally, however, since the binding energy for the ground state of Au–He is very low, observing this species would be challenging.

7.2.2 The Au (6p) states

The Au-He complexes were calculated, as in previous Chapters, using a series of CASSCF+MRCI calculations, including the Davidson correction (+Q) with an aug-cc-pVQZ basis set, where the 5*d* and lower orbitals of Au were constrained to remaining doubly occupied. As such, only the unpaired 6*s* or 6*p* electron was allowed to be active in the calculations for the respective states. However, the doubly-occupied orbitals were allowed to relax during the CASSCF procedure.

This did, of course, limit the amount of dynamic correlation included; however, this was satisfactory since only a qualitative picture was needed. Since the CASSCF treatment does not consider the same set of orbitals for the $^2\Sigma^+$ and $^2\Pi$ states (because of the different symmetry), the calculated asymptotic energies were not precisely equal for the $D^2\Pi$ and $E^2\Sigma^+$states.

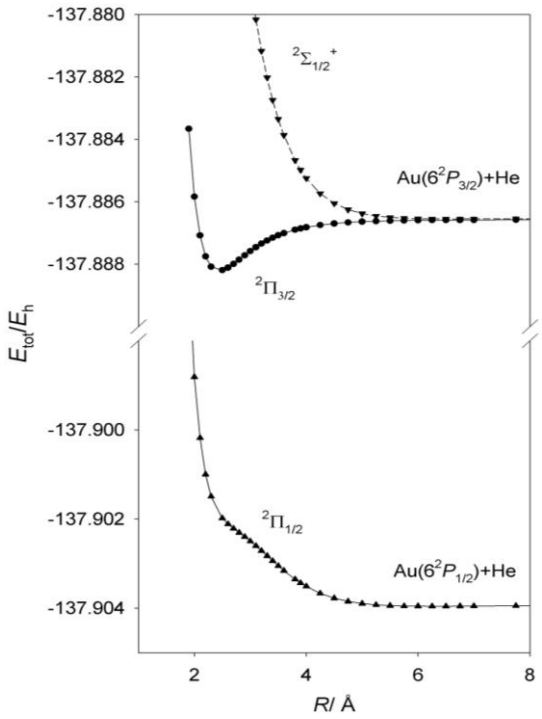

Figure 7.1. CASSCF+MRCI+Q/aVQZ calculations for the $D^2\Pi_{1/2}$, $D^2\Pi_{3/2}$ and $E^2\Sigma_{1/2}{}^+$ states of Au-He.

In the Chapters 3-5 the Davidson-corrected CASSCF + MRCI + Q energies of the two $^2\Pi$ states and the $E^2\Sigma^+$ state were used as the unperturbed energies in state-averaged CASSCF spin-orbit calculations, to determine the spin orbit coupling at each *R*. However, this resulted in a calculated separation value for the spin-orbit split asymptotes of 2500-2600 cm^{-1}, considerably lower than the $6^2P_{3/2}$–$6^2P_{1/2}$ atomic splitting of $^3/_2\zeta$ = 3815.4 cm^{-1} (known from atomic

spectroscopy).[17] Although it would be possible to extend these calculations, it has not been done here as a fuller theoretical treatment ought to include a full account of spin-orbit coupling, and hence possible couplings with other $\Omega = {}^{1}/_{2}$ and $\Omega = {}^{3}/_{2}$ states, and perhaps allowing for relaxation of the spin-orbit wavefunctions. Therefore, in this work on Au-He, as in the work for Au-Ne in Chapter 6, analytic expressions (together with the above value of ζ) which link the $^2\Sigma^+$ and $^2\Pi$ states to the spin-orbit states, have been used; the derivation of which are included in the appendix of reference 18. Again, there is a slight non-degeneracy in the $^2\Sigma^+$and $^2\Pi$ states at the asymptotes, and so the $^2\Pi$ state is shifted to match the asymptotic energy of the $^2\Sigma^+$ state prior to employing the analytic expressions. The resulting curves are presented in Figure 7.1. As can be seen it appears that the $D^2\Pi_{1/2}$ state potential is repulsive over a wide range of R owing to a strong spin-orbit interaction with the $E^2\Sigma_{1/2}^+$ state as observed in the other Au-RG complexes.

It is difficult to compare the experimental spectra for the Au(6*p*) states of the Au-RG directly, since very different behaviour is observed in each case. For Au–Ne, the $D^2\Pi_{1/2}$ state is not observed, whilst for Au-Ar there is a significant perturbation of the $D^2\Pi_{1/2}$ state to high v' and a long progression in the $D^2\Pi_{3/2}$ spectrum. In Au–Kr, there is a long progression in the $D^2\Pi_{1/2}$ spectrum, but a severely curtailed one for the $D^2\Pi_{3/2}$ state. For Au–Xe there is a long progression in the $D^2\Pi_{1/2}$ spectrum, containing a severe drop in intensity in the centre of the spectrum, with only a single vibrational feature recorded for the

$D^2\Pi_{3/2}$ state. For Au-Xe the $\Xi_{1/2}$ spectrum residing close to the (Au) $^2P_{3/2} \leftarrow {}^2S_{1/2}$ atomic transition, attributed to the mixing of the $E^2\Sigma_{1/2}^+$ and a $^4\Pi_{1/2}$ state arising from a higher asymptote, was also recorded. Despite these differences, the majority of the observed spectroscopy can be rationalized by three main effects, which are evident from the ab initio calculations employed.

The first of these effects is the mixing of the $E^2\Sigma_{1/2}^+$ state with the $D^2\Pi_{1/2}$ state, leading to the perturbation of the $D^2\Pi_{1/2}$ spectrum of Au–Ar (Chapter 3). Note that the same interaction is occurring for Au–Kr and Au–Xe, according to the calculations reported in Chapters 4 and 5, but the most significant effects appear to be outside the FC window. In Au–Ne (Chapter 6), this mixing leads to a very weakly bound $D^2\Pi_{1/2}$ state and leads to very small FCFs to any bound levels. The calculations reported in Figure 7.1 indicate that similar mixing will occur for the Au–He $D^2\Pi_{1/2}$ state.

The second effect is the interaction of the $D^2\Pi_{3/2}$ state with lower-lying states proposed to be those arising from the lower Au(5^2D) + RG asymptote, in particular the $A^2\Delta_{3/2}$ state. For Au–Kr (Chapter 4), it was concluded that the interaction between the $A^2\Delta_{3/2}$ and $^2\Pi_{3/2}$ states causes the predissociation of the higher v' states, leading to the severely shortened progression, a conclusion that was supported by FC simulations performed. For Au–Xe, the $A^2\Delta_{3/2}$ state crosses in the bound region of the $D^2\Pi_{3/2}$ state, causing predissociation of all but one vibrational level. It was noted in Chapter 5 that the $A^2\Delta_{3/2}$ and $D^2\Pi_{3/2}$

states differed by more than a single electron excitation, which would not be consistent with efficient coupling of these states, and hence the known mixing of the $6^2P_{3/2}$ states with the higher $^4P_{3/2}$ one[19,20] was invoked. An additional effect, only observed in the case of Au–Xe, was the severe disruption of the intensity distribution in the centre of the $D^2\Pi_{1/2}$ spectrum. It was hypothesized that this was caused by weak predissociation *via* the repulsive region of the $B^2\Pi_{1/2}$ state leading to only a partial loss of intensity. The difference between the degrees of predissociation observed for the $D^2\Pi_{1/2}$ and $D^2\Pi_{3/2}$ states of Au-Xe was attributed to the larger energy gap between the $6^2P_{1/2}$ and $^4P_{1/2}$ states in comparison to that of the $6^2P_{1/2}$ and $^4P_{3/2}$ states.

The third factor is the involvement of the higher states arising from the Au($^4P_{5/2}$) + RG ($^1S_0$) asymptote; as previously mentioned in Chapter 1 the Au ($^4P_{5/2}$) state is located only 988.9 cm^{-1} above the Au ($^2P_{3/2}$) state.[21] The involvement of these states is only apparent for Au-Xe in which the mixed character $\Xi_{1/2}$ state is observed close to the Au $^2P_{3/2} \leftarrow {}^2S_{1/2}$ atomic transition. It is the stronger interaction of the $^4\Pi_{1/2}$ states arising from the Au($^4P_{5/2}$) + RG ($^1S_0$) asymptote in the Au-Xe complexes states that allow the potential to impinge on the $E^2\Sigma_{1/2}^+$ spectral region; in the other Au-RG complexes these states are not sufficiently bound to reach this spectral region.

To enable a comparison between the R_e and D_e values of the Au-RG $D^2\Pi_{3/2}$ states the results obtained from RCCSD(T)/*d*-aV∞Z calculations (see Chapter 3-6 for details) for the $D^2\Pi$ state, which should be largely representative of the $D^2\Pi_{3/2}$ state, are presented in

Table 7.2 together with corresponding values for the Au^+–RG species, taken from reference 22 for RG = Ne–Xe, and Au^+–He values taken from reference 18. It is immediately obvious that the trends for the $^2\Pi$ states are not as expected, with the Au–Ne species having the longest bond length and the smallest D_e value. In contrast, the trends in the corresponding parameters for the cations are more in line with expectations with D_e increasing with the increasing size, and hence polarizability, of the complexing RG. As noted in the discussion on the $X^2\Sigma_{1/2}^+$ state, "unexpected" trends are seen for species where there are unpaired valence electrons, and of course that is the situation here, with the $D^2\Pi$ state comprising a closed-shell cationic core, with an unpaired electron in the $6p\pi$ orbital. One rationale for the departure from the expected trend is to note that He does not have any *p* electrons, and hence there is no $p\pi$ (nor $p\sigma$) electron repulsion here, only repulsion that arises from the 1*s* electrons; in contrast, Ne has both *s* and *p* electrons, and so there is "additional" repulsion in the case of Ne, over that of He. These effects have been discussed in some detail previously[23] for the corresponding states of Li–RG and Na-RG. For the larger rare gases, again there are *p* electrons, but there is also the large increase in polarizability over that of Ne, which counteracts the repulsion effect. As support for this, it can be noted from Table 7.2 that the differences in R_e between the $D^2\Pi$ states and ions are: He, 0.004; Ne, 0.391; Ar, 0.121; Kr, 0.083; Xe, 0.032. These are consistent with Ne having strong $p\pi/p\pi$ repulsion, but with this repulsion being compensated by the higher attraction in the cases of Ar, Kr, and Xe. In line with comments in Chapter 5 and reference 22, it is suggested that there may be a coordinate-covalent chemical

component to the binding in the heaviest species. It is worth noting in passing that the Au^+–He and Au-He($D^2\Pi$) bond lengths are almost equal. In fact, in the cases of Li–He and Na–He,[23] the excited neutral $^2\Pi$ state actually had a *larger* D_e value than the cation, attributed to the very large and polarizable excited *p* orbital.

Table 7.2. CASSCF+MRCI+Q+SO values of Δ/ζ for Au–RG at the minima of the $D^2\Pi_{3/2}$ curves. Also included are the RCCSD(T)/*d*-aVQZ R_e and D_e values for the $D^2\Pi$ excited state neutral and $X^1\Sigma^+$ ground cationic states.

Au–RG	Δ/ζ	$R_e(D^2\Pi)$/ Å	$R_e(X^1\Sigma^+)$/ Å	$D_e(D^2\Pi)$	$D_e(X^1\Sigma^+)$
Au–He	1.25	2.413	2.409	379.8	417
Au–Ne	0.45	3.083	2.692	178.2	619
Au–Ar	1.58	2.621	2.500	1960.8	4016
Au–Kr	1.62	2.614	2.531	3546.5	6489
Au–Xe	1.80	2.630	2.598	6918.3	10529

7.2.3 Hunds case (a)/(c) discussion

If it is assumed that the spin-orbit splitting in these Au-RG complexes is mainly due to the "heavy" Au atom, then it can be expected at long *R*, where the interaction between the Au and the RG is weak, then Hund's case (c) coupling of the angular momenta is applicable. As *R* decreases the interaction gets stronger and the electronic angular momenta will gradually couple to the internuclear axis resulting in a shift away from Hund's (c) towards Hund's case (a). The extent of this shift is dependent on the ratio of the energy difference between the $^2\Sigma^+$ and $^2\Pi$ states, Δ, of the diabatic states at separation, *R*, and the spin-orbit coupling constant, ζ. Close to the atomic asymptote where Hund's case (c) is expected, Δ/ζ will be close to 0 while for Hund's case (a) the value is closer to ζ. To get an idea to the extent of evolution to Hund's case (c) for the Au(6*p*)–RG states, the value of Δ/ζ has been

calculated from their respective CASSCF+MRCI+Q curves at the R_e value of the $^2\Pi$ (= $D^2\Pi_{3/2}$) state, the results of which are reported in Table 7.2. As may be seen Au–Ne is the closest to the Hund's case (c) limit at $R_e(D^2\Pi)$, which accounts for the strong mixing with the $E^2\Sigma^+$ state when spin-orbit coupling is present. It is then notable that there is a marked move towards Hund's case (a) for the heavier Au–RG species, bearing in mind the fast changeover as Δ/ζ increases displayed in Figure 7.2, in which the spin-orbit splitting between the $^2\Pi_{3/2}$ and $^2\Pi_{1/2}$ states is given by S.

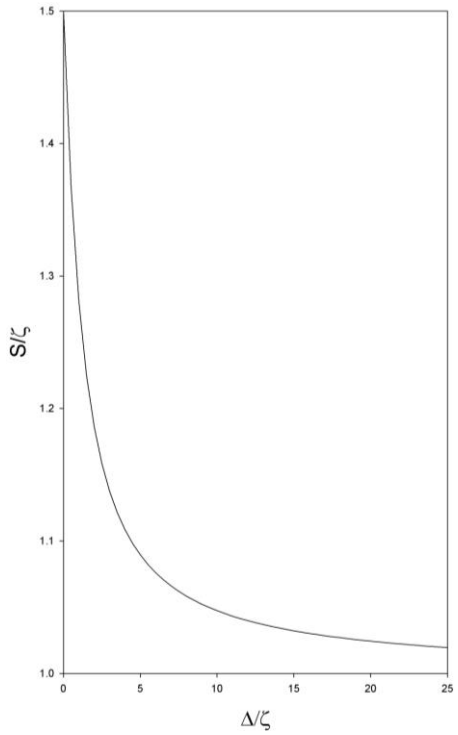

Figure 7.2. Graph showing how Δ varies with respect to *S*; each normalized to the spin-orbit splitting parameter, ζ.

This evolution of Hund's case (c) to Hund's case (a) as R decreases in the heavier RG can be observed experimentally for Au-Kr from the variation in the separation between corresponding v' levels in the $D^2\Pi_{1/2}$ and $D^2\Pi_{3/2}$ states (Table 7.3). As can be seen from Table 7.3

the spin-orbit splitting is decreasing as a function of v', falling from 3133.7 cm^{-1} at v' =26 to 3020.4 cm^{-1} at v' = 22 becoming progressively closer to the pure Hund's case (a) separation of 2543.6 cm^{-1}, which is 2/3 of the atomic term difference ($^3/_2\ \zeta_{6p}$ = 3815.4 cm^{-1}) and hence further from the pure Hund's case (c) value equal to $^3/_2\ \zeta_{6p}$. The experimentally derived equilibrium separation of 2723 cm^{-1} (in which values for T_0 were obtained through a Morse analysis) gives a ratio of 0.71 very close that in pure Hunds case (a). Unfortunately this type of analysis is not possible for any of the other Au-RG species as Au-Kr is the only species in which corresponding v' levels were observed and identified for both of the $D^2\Pi_\Omega$ states.

Table 7.3. Variation in separation of $D^2\Pi_{1/2}$ and $D^2\Pi_{3/2}$ states of ^{197}Au-^{84}Kr as a function of v'. Ratio is that of the separation to the atomic value of 3815.4 cm^{-1}.

v'	Separation (cm^{-1})	Ratio
22	3020.4	0.792
23	3046.6	0.798
24	3074.8	0.806
25	3103.8	0.814
26	3133.7	0.821

That these species are evolving so quickly towards Hund's case (a), despite the low value of the dissociation energy relative to the spin-orbit splitting of $^3/_2\zeta$ (=3814.5 cm^{-1}), can be attributed to the large size of the Au 6*p* orbital relative to the internuclear separation. This causes a large $^2\Pi$–$^2\Sigma^+$ splitting, primarily because of the difference in the behaviour of the binding energy of the two states.

It is worth commenting on the surprisingly high value of Δ/ζ for Au–He, which is significantly higher than that of Au–Ne. This difference can be attributed to the much shorter equilibrium internuclear separation in the lighter species and the consequently larger value of Δ.

The specific expressions for the mixing between the "molecular" states arising from the atomic asymptotes Au (6^2P_J) + RG ($^1S_0$) were derived by Professor Michael Morse at the University of Utah and can be found in the Appendix of reference 18.

7.3 Velocity map imaging work

The most recent work on the Au-RG complexes has been carried out using velocity map imaging techniques. This work was carried out in collaboration with Dr. Stuart Mackenzie's group, specifically Dr. W. Scott Hopkins at the University of Oxford in which a similar experimental set-up to that reported in previous[24] work was employed. The aim of the study was to investigate the predissociation occurring for the Au-Kr and Au-Xe complexes as discussed in Chapters 4 and 5. A brief discussion of the work is given below outlining the mechanism for predissociation of the Au-Xe $\Xi_{1/2}$ state in addition to the method used to determine D_0'' values for the Au-Ar, Au-Kr and Au-Xe complexes. A more detailed account of this study can be found in reference 25.

7.3.1 Au-Xe

Initial REMPI scans in the 41000 – 42000 cm^{-1} spectral region showed that the spectrum recorded for Au-Xe in Chapter 5 in the Au^+-Xe channel could also be simultaneously observed in the Au fragment (Au^+) mass channel. A number of velocity map images of Au^+ were taken for each of the observed vibrational levels from which total kinetic energy release (TKER) spectra were obtained. As can be seen in Figure 7.3, analysis of the TKER spectra shows a perfect correlation between the increased excitation energy and the additional kinetic energy released, and hence the fragmentation can be concluded to be the result of a one photon process. As the initial excitation is to bound levels, fragmentation must occur through predissociation to a degenerate continuum. From extrapolation of the TKER spectrum back to zero, as shown in Figure 7.3, the identity of the continuum was determined to be that of Au($^2P_{1/2}$) + Xe($^1S_0$). It is the absorption of a further photon by the Au($^2P_{1/2}$) fragment that results in the observed Au^+ signal. Using the identity of the continuum, determined through extrapolation of the TKER spectrum back to zero, in addition to the atomic energy transition and the known excitation energy D_0'', can be estimated to be 636±27 cm^{-1}.

The ratio of the peak intensities for the simultaneously observed Au^+-Xe and the Au^+ REMPI spectra mass channels showed that predissociation to the dissociation continuum was relatively efficient for the v' = 8 -13 levels. However, for the v' = 14 level (not observed in the original study at Nottingham) this ratio increased dramatically and was shown to be highly isotopomer specific; the ratio going from ~1.5

for the heavier Au-^{132}Xe, Au-^{134}Xe and Au-^{136}Xe isotopomer to >9 for the lighter ones. Further peculiarities were observed for the v' =14 peaks in that unlike the other observed vibrational levels the peaks were distinctly asymmetric, with a distinct change in this asymmetry as you move to the lighter isotopomers. TKER spectra of the v' = 14 region indicated the fragmentation in this level did not proceed *via* the same mechanism as the other vibrational levels with the intensity of the TKER peak identified as the Au($^2P_{1/2}[5d^{10}6p]$) + Xe($^1S_0[5p^6]$) product channel decreasing concurrently with the rise in intensity of a lower TKER peak corresponding to the Au($^2P_{3/2}[5d^{10}6p]$) + Xe($^1S_0[5p^6]$) product channel. In an attempt to observe this channel directly images were acquired at various photolysis wavenumbers above the v' = 14 level, however, no signal was observed in either of the Au($^2P_{1/2}[5d^{10}6p]$) + Xe($^1S_0[5p^6]$) or Au($^2P_{3/2}[5d^{10}6p]$) + Xe($^1S_0[5p^6]$) product channels, suggesting that there is no transition probability for direct excitation to either continuum.

The conclusion that can be drawn from this evidence is that for the $\Xi_{1/2}$ state potential, as commented on in Chapter 5, there is a small barrier to dissociation to the Au($^2P_{3/2}$) + Xe($^1S_0$) asymptote predicted to arise at the avoided crossing between the $E^2\Sigma_{1/2}^+$ state $^4\Pi_{1/2}$ state correlating to the Au($^4P_{5/2}$) + Xe($^1S_0$) asymptote. As the top of this barrier is approached the coupling to the Au($^2P_{3/2}$) + Xe($^1S_0$) continuum increases. It appears that the v' = 14 level is just below the top of this barrier resulting in a dramatic increase in the amount of coupling on moving from the heavier Au-Xe isotopomers to the lighter ones. In light of this apparent barrier to dissociation the Au-Xe D_0'' value can

be refined to 607 ±5 cm^{-1}, a value in good agreement with the value of 580 cm^{-1} predicted in Chapter 5.

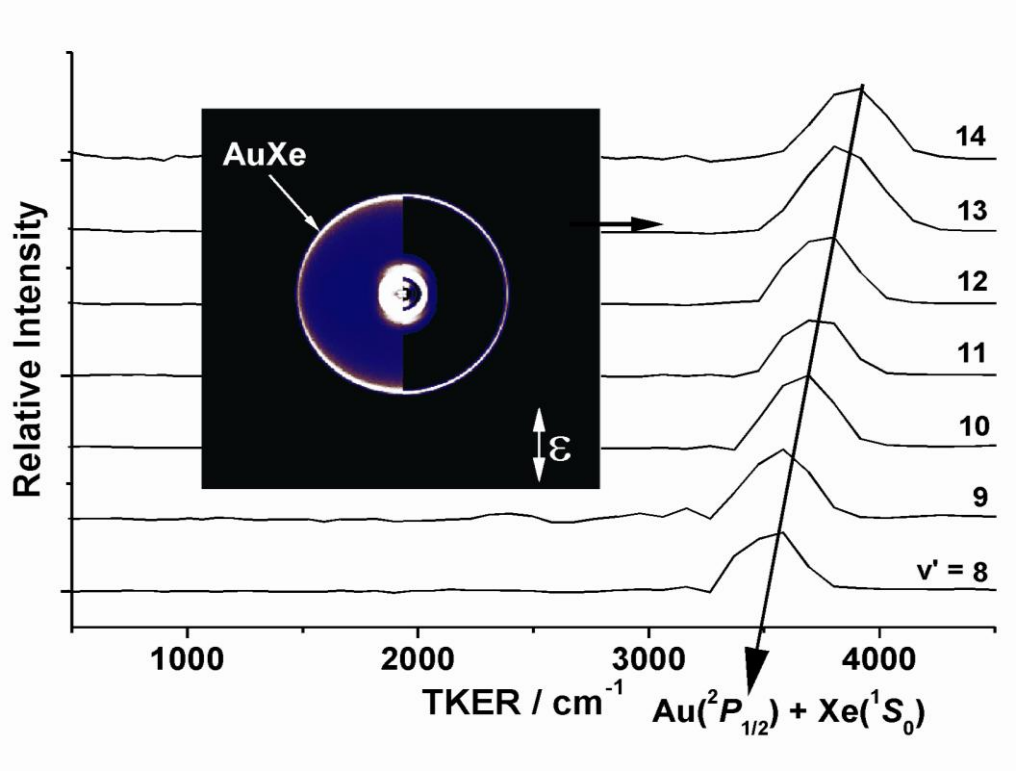

Figure 7.3. (inset) The Au fragment image observed following excitation of the Au-Xe $\Xi_{1/2}$ (v´=13) level. The left hand side shows the raw image, the right hand side the result of the image reconstruction. The smaller less-well resolved rings at the centre of the image are Au atoms produced in direct dissociation of Au-Ar which is produced simultaneously with Au-Xe. The main figure shows the extracted TKER spectra observed by imaging the Au fragment following excitation of each Au-Xe $\Xi_{1/2}$ (v´) level. Extrapolation to zero TKER confirms that predissociation occurs into the Au ($^2P_{1/2}$) + Xe ($^1S_0$) channel. This diagram was produced by Dr. W. Scott Hopkins and used with the permission of Dr. Stuart Mackenzie.

For the lower vibrationals levels it appears that the predissociation observed occurs *via* coupling between the $\Xi_{1/2}$ state and the $D^2\Pi_{1/2}$ state continuum, which can interact with the $\Xi_{1/2}$ state (*via* the $E^2\Sigma_{1/2}^+$ contribution) through spin-orbit interactions. This type of interaction

is consistent with the observations for the Au-RG $D^2\Pi_{1/2}$ states in previous chapters.

7.3.2 Au-Ar and Au-Kr

The ground states of the Au-Ar and Au-Kr complexes each have a smaller binding energy than that of Au-Xe, therefore excitations to the 41600 ± 200 cm^{-1} region promoted transitions directly to the dissociative continuum above the Au($^2P_{3/2}[5d^{10}6p]$) + RG($^1S_0[3p^6]$) threshold and total energy balance calculations are in excellent agreement with this process. This is in direct contrast to Au-Xe where no transition probability to the dissociative continuum was observed. Also in contrast with Au-Xe is the fact that both Au-Ar and Au-Kr show no evidence of photodissociation below the Au($^2P_{3/2}[5d^{10}6p]$) + RG($^1S_0[3p^6]$) threshold.

For both the Au-Ar and Au-Kr complexes D_0'' was determined in a similar manner to that described for Au-Xe. The value of D_0'' for Au-Ar was found to be 149 ± 13 cm^{-1} in good agreement with the value calculated value of 160 cm^{-1} in Chapter 3, and is within 2σ of the current best theoretical value of 171.8 cm^{-1} in which all the non ECP electrons of Au were correlated. However, for Au-Kr the agreement was not quite as good with the D_0'' value of 240 ± 19 cm^{-1} being just outside 2σ the value of 288 cm^{-1} calculated in Chapter 4.

7.4 Trends down the Coinage metal – RG series

In order that trends down the CM-RG series can be discussed calculations similar to those described herein for the Au-RG complexes have recently been performed for the Cu-RG and Ag-RG complexes,[9] the results of which are shown in Table 7.4. From the Table it can be seen that D_e of the CM-RG $X^2\Sigma_{1/2}^+$ state increases with the increasing mass of the coinage metal. On inspection of the polarizabilites of Cu, Ag and Au (6.1×10^{-24} cm^3, 7.2×10^{-24} cm^3 and 5.8×10^{-24} cm^3) this trend is unexpected as the Au-RG complexes are considerably more bound than the Ag-RG complexes. To rationalize this trend in D_e the R_e values for these complexes have to be considered alongside polarizabilities, for example, in the Ag-RG and Cu-RG complexes R_e is very similar and hence D_e is slightly larger for the Ag-RG in-line with Ag being slightly more polarizable. However, in the Au-RG complexes, R_e is considerably shorter, owing to the relativistic stabilization of the Au 6*s* orbital combined with the lanthanide contraction. This smaller separation has the effect of increasing the magnitude of the dispersive interactions within the Au-RG complexes, resulting in D_e values that are larger than would be expected form polarizabilities alone.

As expected it can be seen in Table 7.4 that D_e values for the $X^2\Sigma_{1/2}^+$ states in the CM-RG complexes increase with the increasing size, and hence polarizability, of the RG. However, the trend observed in R_e is surprising with R_e decreasing continuously from He through to Rn in the Cu-RG and Ag-RG complexes as previously noted for the Au-RG complexes in section 7.2.1 despite the increasing size of the RG atom.

Table 7.4. Summary of theoretically derived spectroscopic constants for the $X^2\Sigma_{1/2}^+$ state of the CM-RG complexes. Constants presented for Cu-RG and Ag-RG complexes are "best" results from reference 9, whilst those for Au-RG are from this work.

Complex	R_e/ Å	D_e/ cm^{-1}	D_0/ cm^{-1}	ω_e/ cm^{-1}	0-1/ cm^{-1}	$\omega_e x_e$/ cm^{-1}
Cu–He[a]	4.603	6.3	1.7	[b]	[b]	[b]
Cu–Ne[a]	4.173	22.0	16.0	12.3	8.9	1.77
Cu–Ar[a]	4.005	90.8	81.5	19.7	0.56	17.3
Cu–Kr[c]	3.935	143.6	134.3	18.9	17.7	0.61
Cu–Xe[c]	3.84	224.4	214.9	19.4	18.6	0.37
Cu–Rn[c]	3.57	334.4	324.2	20.1	19.7	0.19
Ag–He[a]	4.59	7.5	2.2	[b]	[b]	[b]
Ag–Ne[a]	4.13	28.2	21.7	13.6	0.18	10.3
Ag–Ar[a]	4.00	113.8	104.2	19.8	0.68	18.0
Ag–Kr[c]	3.96	169.3	160.3	18.3	17.3	0.48
Ag–Xe[c]	3.93	253.9	244.6	18.7	18.0	0.31
Ag–Rn[c]	3.77	355.8	345.8	20.0	19.5	0.26
Au–He[d]	4.08	15.3	6.1	[b]	6.1	[b]
Au–Ne[d]	3.83	47.2	38.0	19.1	15.1	2.02
Au–Ar[d]	3.73	176.5	163.9	25.8	23.9	0.97
Au–Kr[e]	3.64	284.8	273.0	23.7	22.8	0.48
Au–Xe[e]	3.42	515.5	503. 1	24.7	24.2	0.256
Au–Rn[e]	3.22	820.3	804.1		31.8	

[a] RCCSD(T)/*d*-awCV∞Z (reference 10)

[b] too few levels to allow determination of these constants

[c] RCCSD(Val,T)/*d*-awCV∞Z – Val indicates that only the valence electrons on CM were correlated (reference 9)

[d] RCCSD(T)/*d*-awCV∞Z

[e] RCCSD(Val,T)/*d*-aV∞Z – Val indicates that only the valence electrons on Au were correlated.

For this observed decrease in R_e to occur, the increase in attraction between the CM and the heavier RG atoms must be large enough to overcome the increase in the RG van der Waals radii. In recent studies of the isovalent Ba^+-RG[26] and, Ca^+-RG, Sr^+-RG and Ra^+-RG[27] complexes it was concluded that *sd* hybridization was present leading to electron density moving off the internuclear axis resulting in an increase in the interaction energy. However, for CM-RG, complexes

this type of *sd* hybridization seems unlikely, despite the presence of low lying states ^2D states in Cu and Au and its occurrence in the alkaline metal cations. The rationale for this is that the *sd* hybridization in the Group 2 cations involves the lowest unoccupied *d* orbitals, whereas for the coinage metals, the lowest ^2D states involve a $ns \leftarrow (n\text{-}1)d$ excitation. Mixing of these states would serve to *increase* the amount of *s* electron density around the CM-RG atom. The analogous process as for the alkaline earth cations would require a $nd \leftarrow ns$ excitation on the CM, and this is higher in energy than the $np \leftarrow ns$ excitation. As may be seen from contour plots in Figure 7.4 there is no evidence of *sd* hybridization, however the movement of electron density off the internuclear axis on the approach of the RG atom indicates the occurrence of a small amount of *sp* hybridization within the heavier CM-RG complexes. This *sp* hybridization has the effect of reducing the repulsion between the two sets of valence electrons and deshields the CM cationic core, resulting in a stronger interaction between the two atoms. It is apparent that there is a greater degree of hybridization in the complexes involving the heavier RG atoms allowing to approach closer.

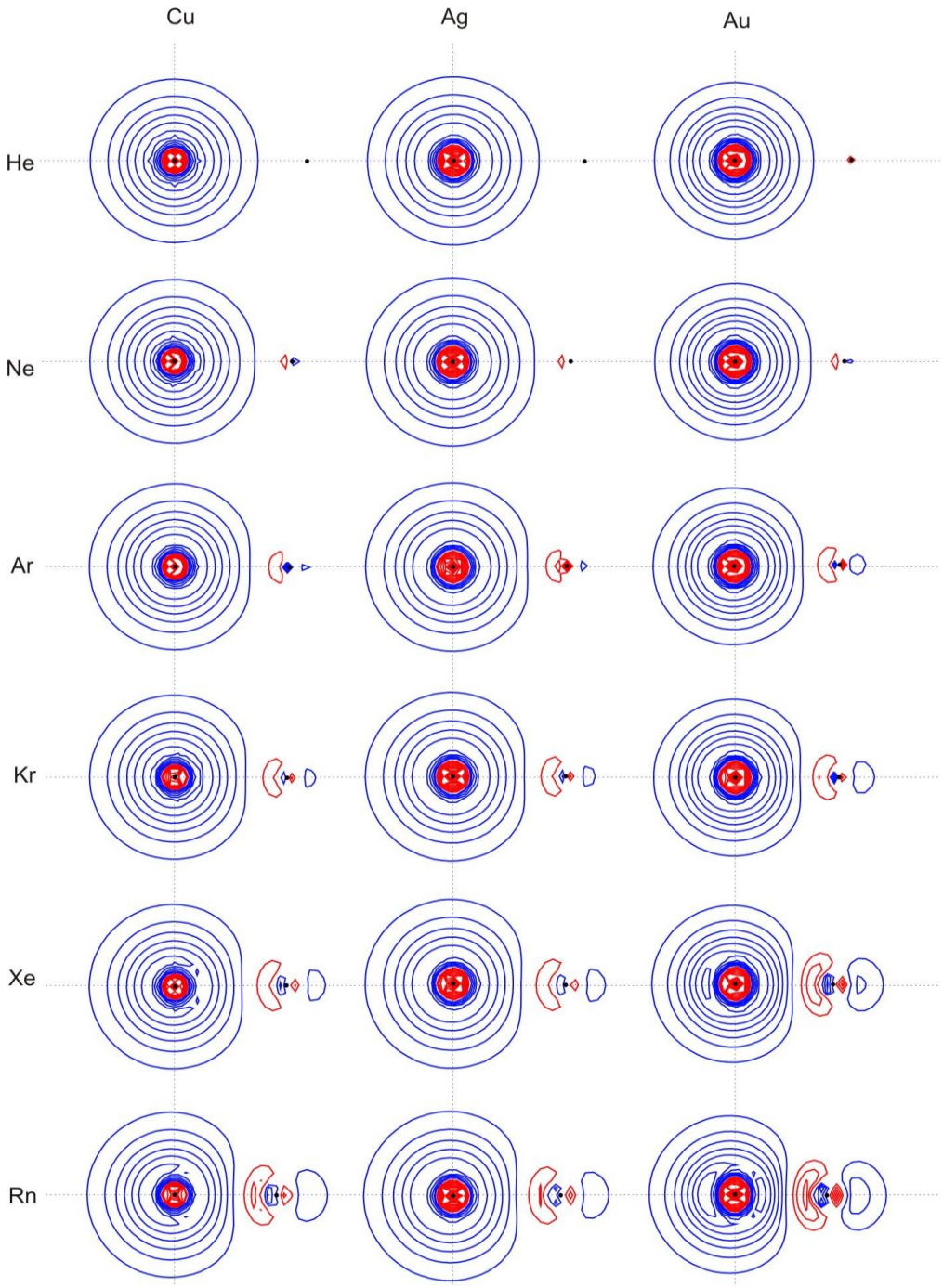

Figure 7.4. MOLDEN contour diagrams of the HOMO for each CM–RG complex calculated at the RCCSD(T) R_e values. The spacings of the contours are constant and were selected to show the details clearly for all complexes. The different colours indicate opposite signs of the wavefunction. Diagram produced by A. M. Gardner.

7.5 Conclusions

The spectroscopy of the Au-RG complexes in the vicinity of the Au $^2P_{1/2,\ 3/2} \leftarrow {}^2S_{1/2}$ atomic transitions has been investigated and it has been shown that the spectroscopy in this energetic region is not as simple as might have been expected. The complicated nature of the observed spectra has lead to *ab initio* calculations being an invaluable aid in their interpretation. Through these calculations it has been shown that this complicated spectroscopy arises from three main effects.

The first effect is the mixing of the $D^2\Pi_{1/2}$ and $E^2\Sigma_{1/2}{}^+$ states through spin-orbit interaction. This mixing leads to the observation of a sudden change in vibrational spacing and rotational band profile for the $D^2\Pi_{1/2} \leftarrow X^2\Sigma_{1/2}{}^+$ transition in Au–Ar. However, the same mixings are not observed in the spectra of the heavier species, since the resulting perturbation in the potential energy curves, lies outside the FC window. For Au–Ne, the mixing leads to an extremely weakly-bound $D^2\Pi_{1/2}$ state, and results in no spectrum being observed.

The second effect is the increasing interaction of lower states, most probably the *A, B* and *C* states, with the *D* and *E* states as the RG gets heavier. This leads to the severe curtailing of the $D^2\Pi_{3/2} \leftarrow X^2\Sigma_{1/2}{}^+$ spectrum for Au–Kr and Au–Xe in which only a single vibronic level is observed for the later species. It also leads to the dramatic loss of intensity in the centre of the $D^2\Pi_{1/2} \leftarrow X^2\Sigma_{1/2}{}^+$ spectrum for Au–Xe. Ideally further VMI studies would be performed to confirm the identity of the interacting states.

The third effect is the involvement of the higher states arising from the Au($^4P_{5/2}$) + RG asymptote leading to the observation of the mixed character $\Xi_{1/2}$ state for Au–Xe, close to the energy of the $6^2P_{3/2}$ state. This state is only observed in Au-Xe as at least one of the states is sufficiently bound to enable an avoid crossing with the $E^2\Sigma_{1/2}^+$ state.

In the Au–RG $X^2\Sigma^+$ states, it can be seen that calculated D_e values increase steadily from He to Rn (as is true for essentially all M–RG and M^+–RG complexes studied previously). The calculated R_e values are shown to, rather unexpectedly, decrease steadily from He to Rn, despite the fact that the van der Waals radii of the RG atoms increasing substantially and regularly from He to Rn. Initial evidence suggests that this is a result of the balance between attraction and repulsion, combined with the evolution of *sp* hybridization, making the closer approach of the heavier RG more favourable.

Interestingly, for the $D^2\Pi$ states, an anomalous trend was observed, where the Au–He binding energy is almost twice that of Au–Ne, and there is a dramatic increase in the binding energy from Au–Ne to Au–Ar. The former is explained by the presence of *p* electrons on Ne, which leads to a marked increase in electron repulsion with the Au 6*p* electrons (something that has been discussed previously for Li–He and Na–He[23]); the latter is explained by the larger polarizability of the Ar atom over that of Ne.

Comparison of the Au-RG complexes to the other CM-RG species has shown that the significantly shorter R_e observed in Au-RG complexes,

attributed to relativistic and lanthanide contractions, leads to considerably stronger bonding in these complexes. It is also apparent that a set of reliable experimental values for the Cu-RG complexes to compare to theory is needed as at present the only experimental value for these species appears to be in error.

References

[1] MOLPRO is a package of *ab initio* programs written by H. J. Werner, P. J. Knowles and others.

[2] D. Figgen, G. Rauhut, M. Dolg, and H. Stoll, *J. Chem. Phys.*, 2005, **311**, 227.

[3] K. A. Peterson, D. Figgen, E. Goll, H. Stoll, M. Dolg, *J. Chem. Phys.,* 2003, **119**, 11113.

[4] S. F. Boys, F. Bernardi, *Mol. Phys.,* 1970, **19**, 553.

[5] T. Helgaker, W. Klopper, H. Koch and J. Noga, *J. Chem. Phys.*, 1997, **106**, 9639.

[6] A. Halkier, T. Helgaker, P. Jỳrgensen, W. Klopper, H. Koch, J. Olsen and A. K. Wilson, *Chem. Phy. Lett.*, 1998, **286**, 243.

[7] R. J. LeRoy, LEVEL 7.2 - *A computer program for solving the radial Schrödinger equation for bound and quasibound levels, and calculating various expectation values and matrix elements*. (University of Waterloo Chemical Physics Research Program Report CP-555R (2000)).

[8] D. Bellert and W. H. Breckenridge, *Chem. Rev.* 2002, **102**, 1595-1622.

[9] A. M. Gardner, R. J. Plowright, M. J. Watkins, T. G. Wright, W. H. Breckenridge, *J. Chem. Phys.*, submitted.

[10] R. A. Gottscho, B. Ahmed-Bitar, W. P. Lapatovich, W. P. Renhorn, and D. E. Pritchard, *J. Chem. Phys.*, 1981, **75**, 2546 and references therein.

[11] G. Apfelbach, A. Nunemann, and D. Zimmerman, *Chem. Phys. Lett.*, 1983 **96**, 311.

[12] R. Bruhl, J. Kapetanakis, and D. Zimmerman, *J. Chem. Phys.*, 1991, **94**, 5865.

[13] M. F. McGuirk, L. A. Viehland, E. P. F. Lee, W. H. Breckenridge, C. D. Withers, A. M. Gardner, R. J. Plowright, and T. G. Wright, *J. Chem. Phys.*, 2009, **130** 194305.

[14] E. Qing, L. A. Viehland, E. P. F. Lee and T. G. Wright, *J. Chem. Phys.*, 2006, **124**, Article #044316.

[15] E. P. F. Lee, B. R. Gray, N. A. Joyner, S. H. Johnson, L. A. Viehland, W. H, Breckenridge, and T. G. Wright, *Chem. Phys. Lett.,* 2007, **450**, 19-24.

[16] F. Cargnoni, T Kuś, T. Mella and R. J. Barlett, *J. Chem. Phys.,* 2008, **129**, 204307.

[17] J. C. Ehrhardt and S. P. Davis, J. Opt. Soc. Am., 1971, **61**, 1342.

[18] R. J. Plowright, A. M. Gardner, C. D. Withers, T. G. Wright, M. D. Morse and W. H. Breckenridge, *J. Phys. Chem. A*, 2010, **114**, 9, 3103.

[19] D. M. Gruen, S. L. Gaudioso, R. L. McBeth and J. L. Lerner, *J. Chem. Phys.*, 1974 **60**, 89.

[20] D. Roser, R. Pellow, M. Eyring, M. Vala, J. Lignieres, and J. C. Rivoal, *J.Chem. Phys.*, 1992 **166**, 393.

[21] http://physics.nist.gov/PhysRefData/Handbook/Tables/goldtable5.htm.

[22] W. H. Breckenridge, V. L. Ayles, and T. G. Wright, *J. Phys. Chem. A,* 2008, **112**, 4209.

[23] S. Bililign, M. Gutowski, J. Simons and W. H. Breckenridge, *J. Chem. Phys.*, 1994, **100**, 8212.

[24] W. S. Hopkins, S. M. Hamilton, P. D. McNaughter and S. R. Mackenzie, *Chem. Phys. Letts.*, 2009, **483** (1-3), 10.

[25] W. S. Hopkins, A. P. Woodham, S. R. Mackenzie, R. J. Plowright and T. G. Wright, *J. Chem. Phys.*, submitted.

[26] M. F. McGuirk, L. A. Viehland, E. P. F. Lee, W. H. Breckenridge, C. D. Withers, A. M. Gardner, R. J. Plowright and T. G. Wright, *J. Chem. Phys.*, 2009, **130**(19), 194305.

[27] A. M. Gardner, C. D. Withers, T. G. Wright, T. I. Kaplin, C. Y. N. Chapman, L. A. V Viehland, E. P. F. Lee and W. H. Breckenridge, *J. Chem. Phys.*, (in press)